Open Research Online

The Open University's repository of research publications
and other research outputs

Large-scale changes of the cloud coverage in the Indi Ba,Bb system

Journal Item

How to cite:

Hitchcock, J A; Helling, Ch; Scholz, A; Hodosan, G; Dominik, M; Hundertmark, M; Jørgensen, U G; Longa-Peña, P; Sajadian, S; Skottfelt, J; Snodgrass, C; Bozza, V; Burgdorf, M J; Campbell-White, J; Jaimes, Roberto Figuera; Fujii, Y I; Haikala, L K; Henning, T; Hinse, T C; Lowry, S; Mancini, L; Rahvar, S; Rabus, M; Southworth, J and von Essen, C (2020). Large-scale changes of the cloud coverage in the Indi Ba,Bb system. Monthly Notices of the Royal Astronomical Society, 495(4) pp. 3881–3899.

For guidance on citations see FAQs.

© [not recorded]

Version: Version of Record

Link(s) to article on publisher's website:
http://dx.doi.org/doi:10.1093/mnras/staa1344

Copyright and Moral Rights for the articles on this site are retained by the individual authors and/or other copyright owners. For more information on Open Research Online's data policy on reuse of materials please consult the policies page.

oro.open.ac.uk

Monthly Notices
of the
ROYAL ASTRONOMICAL SOCIETY

MNRAS **495,** 3881–3899 (2020)
Advance Access publication 2020 May 18

doi:10.1093/mnras/staa1344

Large-scale changes of the cloud coverage in the ϵ Indi Ba and Bb system

J. A. Hitchcock,[1,2]★ Ch. Helling,[1,2,3] A. Scholz,[1,2] G. Hodosan,[1,2] M. Dominik,[1,2] M. Hundertmark,[4] U. G. Jørgensen,[5] P. Longa-Peña,[6] S. Sajadian,[7] J. Skottfelt,[8] C. Snodgrass,[9] V. Bozza,[10,11] M. J. Burgdorf,[12] J. Campbell-White,[13] Roberto Figuera Jaimes,[1,14,15] Y. I. Fujii,[5,16,17,18] L. K. Haikala,[19] T. Henning,[20] T. C. Hinse,[21] S. Lowry,[22] L. Mancini,[20,23,24,25] S. Rahvar,[26] M. Rabus,[27,28] J. Southworth,[29] and C. von Essen[30] (The MiNDSTEp Collaboration)

Affiliations are listed at the end of the paper

Accepted 2020 May 6. Received 2020 May 6; in original form 2020 January 20

ABSTRACT

We present the results of 14 nights of *I*-band photometric monitoring of the nearby brown dwarf binary, ϵ Indi Ba and Bb. Observations were acquired over 2 months, with a total of close to 42 h of coverage at a typically high cadence of 1.4 min. At a separation of just 0.7 arcsec, we do not resolve the individual components, and so effectively treat the binary as if it were a single object. However, ϵ Indi Ba (spectral type T1) is the brightest known T-type brown dwarf, and is expected to dominate the photometric signal. We typically find no strong variability associated with the target during each individual night of observing, but see significant changes in mean brightness – by as much as 0.10 mag – over the 2 months of the campaign. This strong variation is apparent on a time-scale of at least 2 d. We detect no clear periodic signature, which suggests that we may be observing the T1 brown dwarf almost pole-on, and the days-long variability in mean brightness is caused by changes in the large-scale structure of the cloud coverage. Dynamic clouds will very likely produce lightning, and complementary high-cadence *V*-band and H α images were acquired to search for the emission signatures associated with stochastic 'strikes'. We report no positive detections for the target in either of these passbands.

Key words: techniques: photometric – brown dwarfs – stars: individual: ϵ Indi Ba and Bb.

1 INTRODUCTION

As brown dwarfs are not massive enough to maintain stable hydrogen fusion, they will inevitably cool with age. Initially, most brown dwarfs are late M dwarfs, but as they evolve they exhibit spectral types of L, T, and Y. As a brown dwarf evolves, the molecular gases in its atmosphere will condense and form clouds. These largely consist of particles made of a mix of silicate, metallic oxide, and iron, whose refractory properties are encoded into the brown dwarf's spectra (e.g. Burrows, Sudarsky & Hubeny 2006; Helling et al. 2008).

The ϵ Indi Ba and Bb brown dwarf binary hosts a T1 (Ba) and a T6 (Bb) component (King et al. 2010). At a distance of only 3.6 pc, ϵ Indi Ba is the brightest known T dwarf. Given this potential for precise photometry, this system provides an excellent case study with which to probe the transition from L to T spectral types. During this stage of a brown dwarf's lifetime, it is likely to exhibit pronounced optical variability, associated with changes in cloud coverage above the photosphere (e.g. Radigan et al. 2014; Metchev et al. 2015; Eriksson, Janson & Calissendorff 2019), with the exact nature of the observable signatures being partly dependent on the inclination angle. For example, rotating spots and weather systems on the surface may be used to infer the rotation periods of these objects when viewed close to the equator. Irregularly evolving time series can result from phase shifts between banded structures on the surface with different periods (Apai et al. 2017). Further, the continued aggregation of condensates on to the surface of the cloud particles may cause the clouds to thin into an optically transparent atmosphere, and ultimately rain-out into the lower, optically thick atmosphere (e.g. Knapp et al. 2004). Time series photometry has proven to be an invaluable tool for monitoring the atmospheric variability of these objects (Apai et al. 2019), and for the past two decades has been successful in measuring both the periodic and quasi-oscillatory signatures seen in both old and young brown dwarfs (e.g. see Scholz & Eislöffel 2004; Artigau et al. 2009) with

★ E-mail: jah36@st-andrews.ac.uk

© 2020 The Author(s)
Published by Oxford University Press on behalf of the Royal Astronomical Society

Downloaded from https://academic.oup.com/mnras/article-abstract/495/4/3881/5838753 by The Open University user on 22 June 2020

surveys both on the ground (Vos et al. 2019) and in space (Biller et al. 2018).

The *I*-band observations presented in this paper were typically acquired at a high cadence of ∼1.4 min. One motivation for probing the short-time-scale variation of this ultracool target is to test for signatures potentially diagnostic of lightning in the atmospheres of the binary's components. Lightning strikes are short, stochastic events that are expected to occur collectively in something like an extrasolar storm (Yang et al. 2016). Since lightning has never been observed on extrasolar objects, the typical duration of individual strikes in brown dwarf atmospheres is unknown. However, individual strikes will likely have a sub-second duration, with e.g. an average duration of 10^{-4} s on the Earth (Volland 2013), and 0.3 s for the slowest Saturnian strikes (Zarka et al. 2004). This, however, can be very different on brown dwarfs and on exoplanets due to different atmospheric chemistries, dynamics, and density structures.

The net behaviour of these strikes can be a brightening of the target in the optical but also in the radio or UV, with a magnitude dependent on the brightness temperature of individual strikes, percentage coverage of the storm over the hemisphere, the rate of strikes, etc. The effects may also manifest as darkening in specific wavelength bands due to chemical changes caused by lightning (see table 1 of Bailey et al. 2014), e.g. due to the occurrence of HCN at the expense of CH_4 (Hodosán, Rimmer & Helling 2016) or more complex molecular ions like HCO^+ suggested in the more rarefied gases of planet-forming discs (Helling et al. 2016). The short, stochastic brightening associated with strikes could be probed by quantifying the asymmetry in the flux of the light curve, provided the signature exceeds the noise, of course.

Extrasolar lightning has never been observed, and if lightning is indeed present on ϵ Indi Ba and Bb, its properties may be very different to that of lightning strikes observed in the Solar system. Planning an ideal strategy to detect strikes is therefore challenging. Chapter 7 of Hodosán (2017) details a parameter study to estimate a range of possible optical fluxes of lightning strikes originating in the atmosphere of ϵ Indi Ba and Bb, and subsequently, the feasibility of observing these strikes with the telescope and filter system used in this work (Section 2). The parameters considered by Hodosán (2017), and the associated equations, are listed in Appendix C. Necessarily, the properties of Solar system lightning must be used, but it is shown that if lightning strikes in the brown dwarf's atmosphere occur over its hemisphere with a flash density (i.e. the rate of strikes per unit area) comparable to that which is observed in the plumes of volcanic eruptions on the Earth, then these strikes would cause an increase in brightness similar to that of the combined brightness of both brown dwarfs, and be easily observed in this study. To take the most promising case as just one example, if we assume that the strikes have power and discharge durations as estimated by Bailey et al. (2014), i.e. (equations C1–C4) $P_{\rm opt,\,fl} = 10^{15}$ W, $\tau_{\rm fl} = 10^{-4}$ s, and occur with a flash density like that observed during the Mt Redoubt Eruption (2009 March 29), $\rho_{\rm fl} = 2000\,{\rm km}^{-2}\,h^{-1}$, over the brown dwarf's entire visible hemisphere, this would result in a signal with an apparent magnitude of about 15.2 and 15.7 in the *I* and *V* bands, respectively. It is thought that the volcanic dusty plumes associated with these very high flash densities may be analogous to the silicate-rich dust clouds present in brown dwarf atmospheres (Helling et al. 2008). A full exploration of the parameter space for the properties of extrasolar lightning on ϵ Indi Ba and Bb is outside the scope of this work, and so we refer the reader to table 7.6 in chapter 7 of Hodosán (2017) for a summary of possible signal strengths.

At a separation of just 0.7 arcsec, the individual components of this binary are rarely resolved with conventional ground-based imaging. As such, in the work presented here, we measure the photometry for the combined system. This is true for all previous studies of the time-varying brightness of this source, which we discuss below.

Following the discovery of the system (Scholz et al. 2003), Koen (2003) obtained 2.3 and 3.3 h of *I*-band photometry on two nights, 4 d apart. A drop in mean magnitude of ∼0.1 mag is seen between the two nights, in addition to an enhanced scatter relative to the comparison stars in each night's time series. A gradual brightening of the target is also seen in both nights, and a 0.05 mag (mag) linear rise is seen over about 3 h.

Soon afterwards, the binary nature of the system was established (McCaughrean et al. 2004). Koen, Matsunaga & Menzies (2004) revisited the target, acquiring 2.9 h of *H*- and *K*-band photometry. Aperiodic scatter, albeit no greater than at the level of 12 mmag is seen in both bands. A period of 3.1 h is shown to fit the concurrent *H* and *K* photometry well, yet given that this exceeds the length of the run, the authors point out that this is clearly not a reliable detection.

Koen (2005) presents 3.6 h of I_C photometry of the target, over which a strong linear brightening is observed, at a rate of 0.75 mag per day (i.e. 0.1 mag over the course of the run). A plot of the residuals of a straight line fit to the trend suggests an additional random component to the variability, which with reference to comparison stars does not likely arise from atmospheric or instrumental effects. This suggested that the 3.1 h period was either transient or incorrect, and supported the variability first described in Koen (2003). Indeed, these results taken together suggested that ϵ Indi Ba and Bb shows comparable levels of variability on both days-long and hourly time-scales. With follow-up K_S differential photometry, Koen et al. (2005) further showed the target to have faded by ∼0.05–0.06 mag between 2003 June and 2004 October.

Point spread function (PSF) photometry was the chosen approach for all of these photometric studies. As discussed in Koen (2009), for unresolved binary systems, stellar magnitudes determined by PSF fitting may be systematically affected by seeing. Therein, it is suggested this effect arises from seeing-dependent PSF variations when observing unresolved binaries with angular separations just below the best resolution limit. With a component separation of roughly 0.7 arcsec, the prior PSF fitting photometry of ϵ Indi Ba and Bb is expected to be strongly affected by this systematic effect. Indeed, Koen (2012) revisits the observations of the target – in addition to obtaining three new sets of ∼3.0 h *I*-band observations – and finds that all the time series show a strong dependence of variability with seeing. Correcting for this, the linear rise seen in Koen (2005) is replaced with a very different, smoothly varying function, and over the now four runs that do in fact show short-time-scale brightness changes, the revised level of variability is shown to be much smaller than previously suggested, with only two nights showing a variation as large as 0.05 mag over a few hours. The conclusion of significant differences in mean brightness between nights, however, still holds, with a range of 0.136 mag over this decade of intermittent *I*-band observations.

In this paper, we present the results of 14 nights of high-cadence, *I*-band photometric monitoring of the combined ϵ Indi Ba and Bb system, acquired over 2 months. In Section 2, we outline the observations, data reduction, and the approach for the differential photometry. The subsequent results are presented in Section 3, followed by a discussion of their astrophysical implications in Section 4. We summarize our conclusions in Section 5.

Downloaded from https://academic.oup.com/mnras/article-abstract/495/4/3881/5838753 by The Open University user on 22 June 2020

Table 1. Spectral classification, effective temperature, bolometric luminosity, and apparent *I*- and *V*-band magnitudes for each component of the ϵ Indi Ba and Bb system (King et al. 2010).

Component	Spectral type	$T_{\rm eff}$ [a] (K)	lg $L/L_{\odot}$	*I*-band (magnitude)	*V*-band (magnitude)
ϵ Indi Ba	T1	1300–1340	-4.699 ± 0.017	17.15 ± 0.02	24.12 ± 0.03
ϵ Indi Bb	T6	880–940	-5.232 ± 0.020	18.921 ± 0.02	$\geq 26.60 \pm 0.05$

Note.[a]Temperature derived by fitting atmospheric models to the observed spectra.

Table 2. Observation inventory for the entire observing campaign.

Date (YYYY-MM-DD)	Number of 'good' images	$t_{\rm exp}$ [a] (s)	Duration of run (h)
2017-07-24	38	120	1.54
2017-08-03	5	60	0.15[b]
2017-08-15	81	60	3.58[c]
2017-08-17	56	60	1.97
2017-08-20	70	60	2.02[d]
2017-08-28	165	60	4.07
2017-08-30	43	80	2.75
2017-09-03	60	60	1.40
2017-09-05	128	60	3.74
2017-09-13	138	60	3.98
2017-09-15	166	60	3.97
2017-09-17	165	60	3.99
2017-09-20	165	60	4.04
2017-09-22	118	60	3.23
2017-09-24	143	60	3.50

Note.[a]Exposure time.
[b]Strong winds meant observations were prematurely aborted. We exclude this night from any further analysis.
[c]Both cloudy conditions and suspected light contamination on the chip from the nearby, bright companion star, ϵ Indi A, produced spurious photometry on this night, resulting in ∼1 h of coverage being clipped. This latter issue is unique to the photometry on this night only (Section 2.2).
[d]Partial interruption of ∼0.5 h, probably due to cloud.

2 OBSERVATIONS AND DATA REDUCTION

2.1 Data acquisition and pre-processing

I-band observations of ϵ Indi Ba and Bb were acquired on 15 separate nights between 2017 July 24 and 2017 September 24 with the Danish 1.54 m telescope (DK1.54) at ESO La Silla, as part of the 2017 MiNDSTEp[1] season. A total of 1457 good[2] *I*-band images were acquired with the Danish Faint Object Spectrograph Camera, which uses a 2K×2K thinned Loral CCD chip with a pixel scale of 0.4 arcsec per pixel, giving a field of view (FoV) of 13.7 arcmin × 13.7 arcmin. Typically, an exposure time of 60 s was used, providing a rapid observational cadence of about 1.4 min. The observing log – which includes the exposure times and total length of each nightly run – is shown in Table 2. Unfortunately, due to high winds, observations were terminated prior to finding the correct pointing on the night of 2017 August 3, and so we exclude these five frames from the analysis (see Section 2.2).

The images were reduced with a bias subtraction and flat-field correction. For most nights, ∼10 biases and 10 *I*-band flats were obtained. All calibration frames were averaged (median), and the master bias and flats were used to reduce the data. For a small number of nights when calibration frames were not obtained, there were always suitable flats and biases acquired either the previous or following day that could be used for the reduction. The SOURCE EXTRACTOR (Bertin & Arnouts 1996) software was used to perform the aperture photometry.

To complement the long-term *I*-band monitoring, intermittent *V*-band and H α observations were acquired at a similarly high cadence with a consistent, 60 s exposure time. Under normal conditions, we do not expect the target to be observable above the background in these passbands with this relatively short exposure time. Rather, the motivation for these observations was to search for signatures that may be associated with stochastic lightning strikes separate from the continuum spectrum of the ultracool target (i.e. the necessarily strong atomic and molecular emission lines at these shorter wavelengths). In Section 4.2, we discuss the results of an analysis of 234 *V*-band and 412 H α images.

2.2 Comparison star selection

An ensemble of stable comparison stars was found with application of the following criteria to each night of observations: (1) The star must be within 2 mag of the target;[3] (2) the standard deviation of the star's magnitudes must be less than that of the target; and (3) the star must appear on at least as many images as the target. This provided a candidate set of 16 comparison stars.

The differential photometry for each night was performed by normalizing the raw comparison star time series by their weighted mean magnitude, and taking the mean across all of the subsequent residual time series. The residual magnitudes may then be subtracted (i.e. a division in flux) from the raw time series of all stars in the FoV. The corrected time series of the comparison stars were then inspected by eye for any signs of variability, and no further cuts were deemed necessary.

To guard against the impact of spurious images on the differential photometry, a 5σ clip was applied to the raw time series of the comparison stars. All sigma clipping described in this work – applied to both the raw and differential photometric time series – is done with respect to the median absolute deviation (MAD) of the scatter in the time series, scaled to a standard deviation,

$$\sigma_{\rm MAD} = 1.4826 \times {\rm median}(|m_i - \tilde{m}|), \quad (1)$$

for magnitudes m_i with median $\tilde{m}$. The factor of 1.4826 is the scaling required for normally distributed data.

It is required that the same ensemble of comparison stars is used for the differential photometry of every data point in our *I*-band time series. This means that if the photometry of just a single member of the ensemble is flagged by the SOURCE EXTRACTOR software for any given frame, the differential photometry for that frame will not be calculated. Typically, no more than 3 per cent

[1]http://www.mindstep-science.org/
[2]Good images are those that have not been flagged for spurious photometry (see Section 2.2).
[3]Brighter stars risk producing diffraction spikes on the CCD

Downloaded from https://academic.oup.com/mnras/article-abstract/495/4/3881/5838753 by The Open University user on 22 June 2020

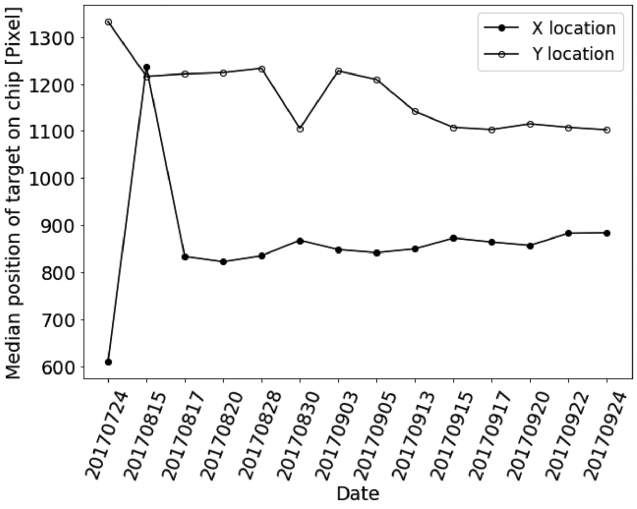

Figure 1. The median X and Y pixel locations for ϵ Indi Ba and Bb for each night of I-band photometry analysed in this work. Following the night of 2017 August 15, a consistent, more easterly pointing was used to ensure that the bright companion star, ϵ Indi A, was not falling directly on the chip.

of all frames acquired on a given night were rejected, with the notable exceptions of the nights of 2017 August 15 and 30 – where the quality of the photometry was severely affected by intermittent cloud coverage for the former, and both cloud coverage and suspected light contamination by ϵ Indi A for the latter – and the night of 2017 August 17, where stars were lost due to an initially inaccurate pointing.

The bright nearby companion star, ϵ Indi A, was visible on the chip for most of the night of 2017 August 15. ϵ Indi A is located west of the target, along the X-axis of the CCD, and for the remainder of the campaign care was taken to ensure that this object was not directly falling on the chip. This is highlighted in Fig. 1, in which we plot the median pixel locations for the target, ϵ Indi Ba and Bb, along the X- and Y-axes of the chip (as a proxy for the pointing), for each night of I-band photometry analysed in this work.

Over all nights of the campaign, we measure a median $\sigma_{\rm MAD}$ of 23 mmag for the target (see Fig. 2).

2.3 Calculation of zero-point offsets

In addition to allowing an examination of variability on minute- to hour-long time-scales, the time coverage of this data set allows an investigation into the variability of ϵ Indi Ba and Bb over almost 2 months. In order to do this, one must calculate the photometric zero-point between different nights of observing to account for the systematic changes in conditions. The simple heuristic approach used here is to calculate the mean shift in magnitude of the reference stars relative to the first night, and apply this shift (i.e. an approximation to the zero-point) to all stars. Here, the difference in mean magnitudes between the first night and night j for comparison star k is written as d_{jk}. The mean shift in brightness over K comparison stars, and the corresponding sample variance, is then equal to

$$\overline{d_j} = \frac{1}{K}\sum_{k=1}^{K} d_{jk}, \quad {S_j}^2 = \frac{1}{K-1}\sum_{k=1}^{K}(d_{jk} - \overline{d_j})^2. \tag{2}$$

It is not guaranteed that reference stars stable over hour-long time-scales are stable over many days, and indeed, two stars were discarded from the 16-large ensemble for calculating zero-points. ϵ Indi Ba and Bb is a very red source, and so second-order colour

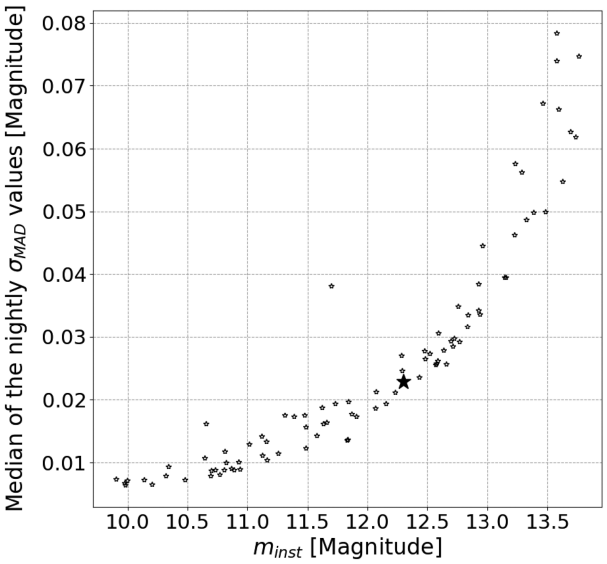

Figure 2. Median instrumental magnitude for ϵ Indi Ba and Bb (large filled star) and other stars in the FoV (small hollow stars) plotted against their median nightly scatter over 14 nights of observations. A variable star with an $m_{\rm inst} \sim 11.7$ is suggested by the plot, and inspection of the within-night time series of this source showed clear, roughly linear rises and falls in brightness of about 0.1 mag over the longest, ∼4 h runs.

effects – which are associated with the wavelength-dependent nature of atmospheric extinction – may be an issue for this target. Encouragingly, however, no clear trend with colour was seen in the reference stars when calculating the zero-point shifts, nor was enhanced scatter in red sources (including the target) seen within nights.[4]

3 GENERAL ASSESSMENT OF VARIABILITY

3.1 Within-night variation

We plot the median instrumental magnitude for the entire zero-point-corrected time series against the median nightly scatter in Fig. 2. The zero-point of the DK1.54 is not well defined, and so the instrumental I-band magnitudes shown here are placed on an arbitrary scale. The $\sigma_{\rm MAD}$ statistic is the MAD of the photometry for each night, scaled to a standard deviation (described by equation 1). ϵ Indi Ba and Bb is shown with the large, filled black star, and all other sources in the field (both comparison stars and field stars) are shown as small hollow stars. This does not suggest any typically enhanced variability on the hours-long time-scales of the individual runs.

The normalized differential photometry for the four nights with the best data coverage is shown in Fig. 3. The target is at the bottom of each of the four panels, represented by the filled circles. For comparison, we plot the light curves for a bright comparison star on the top row (crosses) 2 mag brighter than the target, and a red comparison star of comparable brightness to the target (open circles); see Table 3 for colour and magnitude information. By-eye inspection suggests no greatly enhanced variation in the target relative to the comparison star of similar brightness.

One can, however, see short-time-scale correlated features in the target time series (e.g. see the roughly 15 min-long 'peaked' features

[4]Colour and coordinate information for sources in the FoV was provided by *Gaia* DR2 (Prusti et al. 2016, Brown et al. 2018).

Downloaded from https://academic.oup.com/mnras/article-abstract/495/4/3881/5838753 by The Open University user on 22 June 2020

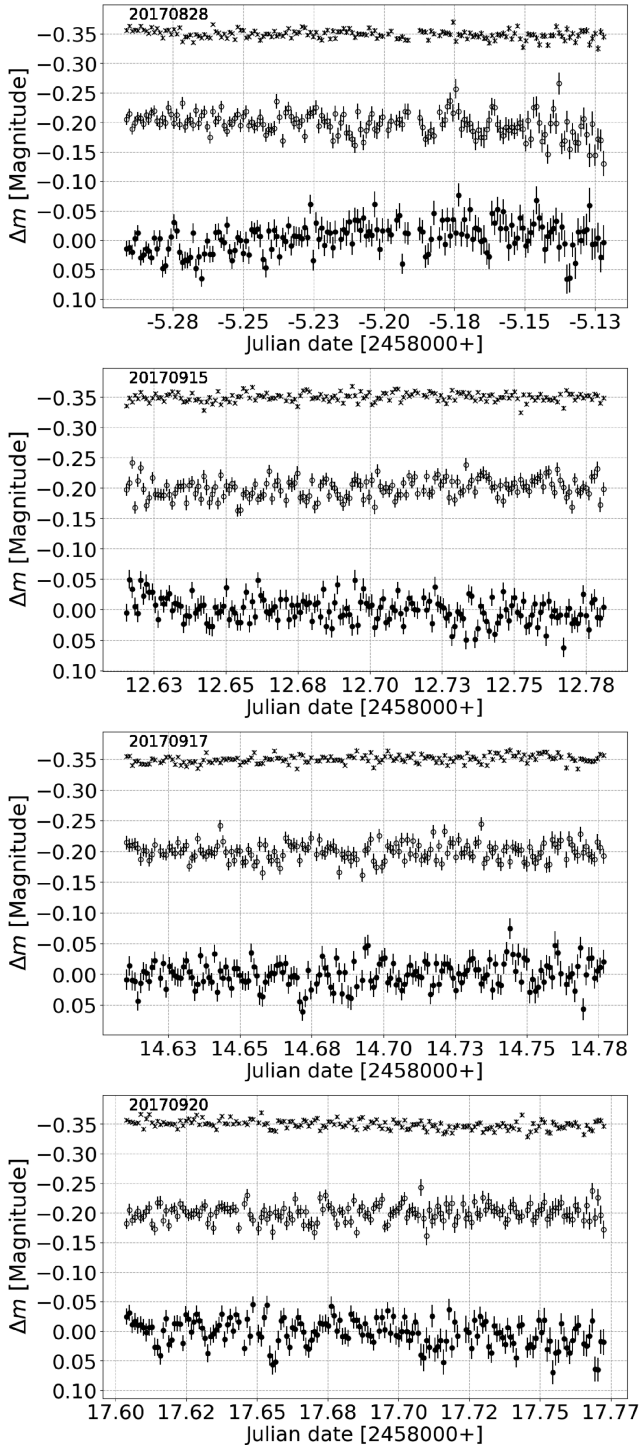

Figure 3. Normalized, arbitrarily offset differential photometry for ϵ Indi Ba and Bb (filled circles), a red comparison star (hollow circles), and a bright comparison star (crosses) on four different nights. The corresponding dates are shown in the top left of each panel as YYYYMMDD.

on the night of 2017 September 17). However, such features are characteristic of correlated noise, which is expected to affect this particularly red source.

The strongest suggestion of any true within-night variability of this target was seen on the night of 2017 August 28 (top panel in Fig. 3), where a gradual rise of about 0.05 mag over the first 2 h is apparent, over which the comparison star time series are flat. In order to ascertain whether this trend could be due to systematic effects, we plot the differential photometry against airmass and image full width at half-maximum (FWHM; as a proxy for the seeing) in Figs 4 and 5, respectively. We fit a straight line to each plot with the usual direct least-squares approach. It is not, however, immediately clear that the relationship between these variables should be linear, and so we empirically estimate an uncertainty for the fit gradient, σ_m with $M = 1000$ bootstrap trials, j, such that

$$\sigma_m^2 = \frac{1}{M}\sum_{j=1}^{M}[m_j - m]^2, \tag{3}$$

where m is the best-fitting gradient when using all the data. This best-fitting parameter and corresponding uncertainty are shown on the graph. Both figures suggest that the photometry is weakly correlated with both airmass and seeing, and the slopes in both instances are significantly different from zero.

To check whether this correlation may be causal, we calculate both correlation coefficients and best-fitting slopes for the two comparison stars listed in Table 3 and directly compare these against the corresponding values for the target. Specifically, we calculate values for both the Pearson correlation coefficient (PCC) and the Spearman rank correlation coefficient (SCC). In order to estimate the uncertainty on the values of these correlation coefficients, we use a Monte Carlo bootstrapping approach to estimate their probability distributions (Curran 2014). To account for the measurement uncertainties in the photometry (which we assume to be normally distributed), for each of the $M = 1000$ bootstrap trials, we perturb the magnitude measurements by adding the measurement uncertainty, Δm_i, multiplied by a number, $\mathcal{G}$, randomly drawn from a Gaussian of mean 0 and variance 1. For each trial, this is done independently for each magnitude measurement, m_i, such that $m_{i,\mathrm{perturbed}} = m_i + \mathcal{G} \times \Delta m_i$. As correlation coefficients are bounded between $[-1, 1]$, their sampling distributions will in general be skewed, and so in this work, we state the median value from the empirically estimated probability distributions as our best estimate of the correlation coefficient, with uncertainties corresponding to the upper and lower 34 percentiles of these distributions.

We note here that the value of the PCC should, in general, be taken with caution for two crucial reasons: (1) Its calculation assumes that the relationship between the variables under investigation really is linear, and (2) it is very sensitive to outliers. Unlike the PCC, the SCC has the advantage of being a measure of *any* monotonic relationship between the two variables, and is far less sensitive to outliers, and so is perhaps the more accurate diagnostic for assessing the strength of any correlation in a situation where second-order colour effects might be present.

In contrast to the target, the comparison stars show weak *positive* trends with airmass and seeing. The correlation coefficients and gradients for each star are shown in Tables 4 and 5. The similar correlation coefficients for the two comparison stars suggest that systematics may be influencing our time series for this night, but in the *opposite* way to how the target appears to be varying. That is, it is possible that we may be in fact underestimating the extent of the brightening over the first part of the night.

On most night, however, the target time series was much more weakly correlated with airmass and seeing, with the typical uncertainty on the gradient being of the same order of magnitude as the gradient itself. None the less, significant, albeit very shallow non-zero gradients are apparent. This is not unexpected, since the

Downloaded from https://academic.oup.com/mnras/article-abstract/495/4/3881/5838753 by The Open University user on 22 June 2020

Table 3. The plotting Key and photometric properties of the three sources – the target and two comparisons stars – shown in the photometric time series in this work.

Source	Key	$m_{\rm inst}$[a]	$(BP-RP)$[b]
Bright comparison star	Crosses	10.144 ± 0.008	1.21
Red comparison star	Open circles	11.730 ± 0.017	2.79
ϵ Indi Ba and Bb	Filled circles	12.300 ± 0.037	6.16

[a]Median instrumental magnitude and associated median absolute deviation (scaled to a standard deviation), for the entire zero-point-corrected time series.
[b]*Gaia* DR2 colour.

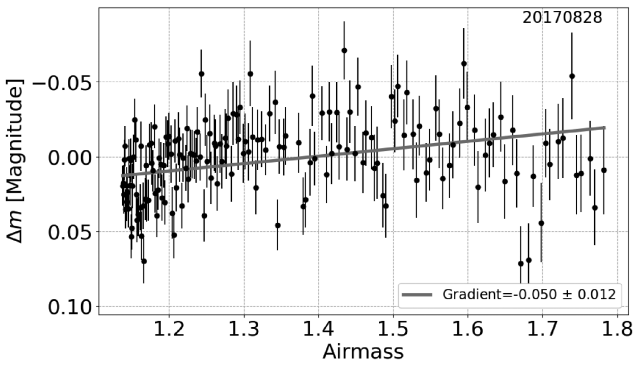

Figure 4. Airmass versus the normalized differential photometry of the target on the night of 2017 August 28. The gradient and corresponding uncertainty of the plotted straight line fit to the data, and the Pearson's correlation coefficient, are shown in the legend.

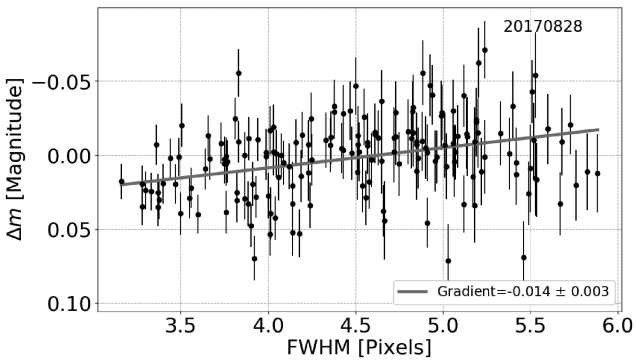

Figure 5. Image FWHM (as a proxy for seeing) versus the normalized differential photometry of the target on the night of 2017 August 28. The gradient and corresponding uncertainty of the plotted straight line fit to the data, and the Pearson's correlation coefficient, are shown in the legend.

comparison stars are necessarily bluer than the target. Importantly though, there is no *consistent* positive or negative linear trend with either airmass or seeing on each night. The plots for the target's differential photometry versus airmass and FWHM for these remaining nights are in Appendix B.

We tabulate these best-fitting slopes alongside the SCC for both the target and a comparison star in Tables B1 and B2.[5] That the SCCs for the comparison star on the majority of nights are consistent with, or very close to 0 within the upper and lower 34 percentiles about the medians of the empirically estimated distributions, suggests that our approach to differential photometry effectively removes these systematic effects. Typically, the target photometry is also weakly correlated with either seeing or airmass. There are, however, a few nights where significant SCCs for the target are apparent, but not for the comparison star. As discussed above, these may too be associated with second-order colour effects, but we cannot rule out the possibility that the target shows small levels of intrinsic variability on these nights, e.g. the nights of 2017 September 20 and 24.

In addition to the night of 2017 August 28, the only other significant within-night variability was seen on the night of 2017 August 15, shown in Fig. 6, but this sudden drop of 0.05 mag is suspect. As discussed in Section 2.2, both intervening cloud and suspected light contamination by ϵ Indi A led to spurious photometry during this night, resulting in an $\sim$1 h interval where there is a gap in the time series, and in the window immediately following this – where we see a sudden drop in brightness of the target – similar behaviour was seen in a number of comparison star time series.

3.2 Search for lightning

No clear short-time-scale signatures indicative of stochastic, 'lightning-like' activity are apparent in the *I*-band time series for all nights (Section 4.2). Additionally, 234 *V*-band and 412 Hα images were fed through SOURCE EXTRACTOR – which was configured with a $>3\sigma$ above background detection threshold – to directly search for strong emission signatures of lightning free from the continuum spectrum of the target. Despite two false positives easily identified as cosmic ray hits, no detections at the position of the target were found in these images.

3.3 Night-to-night variation

ϵ Indi Ba and Bb shows large flux variability over the course of the entire 2 months of observations. The full zero-point shifted light curve of the target is shown on the bottom row of Fig. 9. Therein, we plot both the individual differential magnitudes as the small shaded points, in addition to the mean magnitude and its associated error. The errorbars are the root sum of squares of the standard deviation of the photometry on each night and the error associated with the approximation to the photometric zero-point for each night (see equation 2). For reference, the mean magnitudes of a red comparison star – the same one shown in Figs 3 and 6 – are also plotted.

This red comparison star is both one of the reddest stars in the field and of a similar brightness to the target. That it shows far more stable behaviour in Fig. 9 than the target is supportive of the reality of the variation in the target. Indeed, as described in Section 2.3, there was no clear trend of zero-point with source colour for any of the comparison stars.

[5]For the reasons discussed above, we drop the PCC from these tables, i.e. the relationship between the differential photometry and the parameters under investigation is not necessarily linear.

Downloaded from https://academic.oup.com/mnras/article-abstract/495/4/3881/5838753 by The Open University user on 22 June 2020

Table 4. Table showing the Pearson (PCC) and Spearman (SCC) correlation coefficients and best-fitting slope for the photometry against airmass on the night of 2017 August 28 for the target, and two comparison stars.

Star	Slope (versus airmass)	PCC (versus airmass)	SCC (versus airmass)
Bright comparison star	0.012 ± 0.003	$0.25^{+0.09}_{-0.09}$	$0.24^{+0.08}_{-0.08}$
Red comparison star	0.037 ± 0.008	$0.30^{+0.10}_{-0.09}$	$0.29^{+0.09}_{-0.09}$
ϵ Indi Ba and Bb	-0.050 ± 0.012	$-0.18^{+0.10}_{-0.10}$	$-0.27^{+0.08}_{-0.09}$

Table 5. Table showing the Pearson (PCC) and Spearman (SCC) correlation coefficients and best-fitting slope for the photometry against FWHM (as a proxy for seeing) on the night of 2017 August 28 for the target, and two comparison stars.

Star	Slope (versus FWHM)	PCC (versus FWHM)	SCC (versus FWHM)
Bright comparison star	0.004 ± 0.001	$0.31^{+0.07}_{-0.09}$	$0.29^{+0.09}_{-0.08}$
Red comparison star	0.009 ± 0.002	$0.27^{+0.09}_{-0.09}$	$0.28^{+0.09}_{-0.09}$
ϵ Indi Ba and Bb	-0.014 ± 0.003	$-0.24^{+0.08}_{-0.09}$	$-0.26^{+0.10}_{-0.09}$

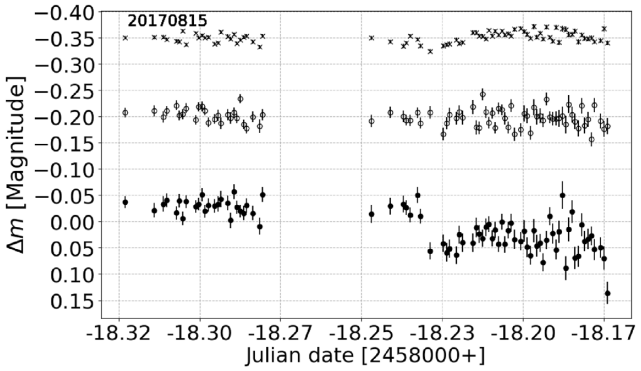

Figure 6. Normalized, arbitrarily offset differential photometry for ϵ Indi Ba and Bb (filled circles), a red comparison star (hollow circles), and a bright comparison star (crosses) on the night of 2017 August 15. Both intermittent cloud coverage and suspected light contamination from ϵ Indi A produced spurious photometry on this night, causing the gap in coverage. For these reasons, the 0.05 mag drop in brightness of the target is assumed to not be real.

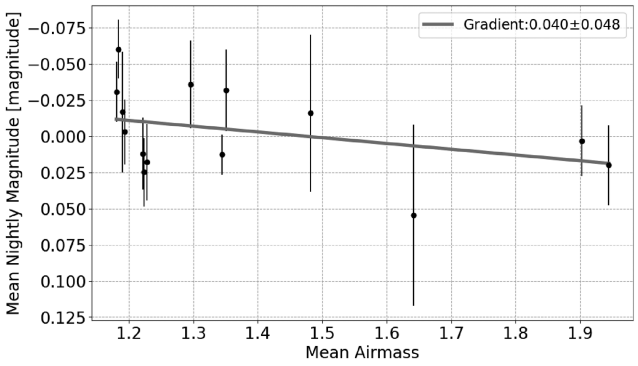

Figure 7. Mean airmass versus the mean value of the normalized differential photometry of ϵ Indi Ba and Bb for each night.

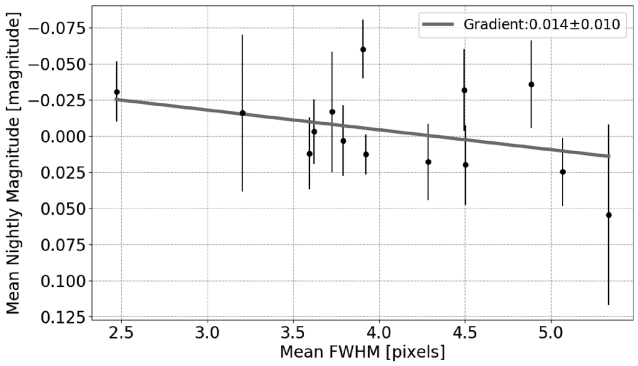

Figure 8. Mean image FWHM (as a proxy for seeing) versus the mean value of the normalized differential photometry of ϵ Indi Ba and Bb for each night.

ϵ Indi Ba and Bb spans a range of 0.10 mag over the whole campaign. There is an ∼0.1 mag increase in brightness over just 4 d, consistent with the previously reported variability in the *I* band described in Section 1. There is no clearly consistent time-scale for this large variation. For example, after JD (245 8000+) 10 the target fades by ∼0.07 mag rapidly over just 2 d, which is immediately followed by a period of relative stability over the next 5 nights covering the last 9 d of the campaign.

Since colour effects are non-linear, it is possible that even small variations in night-to-night systematics may cause large changes in the mean nightly photometry of this very red target. As pointed out in Section 2.2, the photometry on the night of 2017 August 30 was affected by changing cloud coverage, and the mean brightness of several field stars was also seen to vary in a similar manner to the target on this night. If one excludes the nights where clouds are known to have affected the observations (i.e. the nights of 2017 August 15, 20, and 30), we still measure significant variability on a time-scale of at least 2 d, although the net change in brightness over the entire campaign is slightly reduced, at ∼0.09 mag.

As in Section 3.1, we check whether the mean variation in magnitude of the target is correlated with airmass and/or seeing by plotting the mean zero-point shifted magnitude for each night against the corresponding mean values of airmass and FWHM in Figs 7 and 8, respectively. Use of either the Pearson or Spearman correlation coefficients for such small samples is a biased estimate of correlation, and can give spurious results. We see, however, that there is a large relative uncertainty on the gradient of the best-fitting line for both plots, which is again estimated empirically by the bootstrap method with 1000 trials (see equation 3). In Fig. 7, the uncertainty exceeds the gradient itself and so is consistent with a flat line. For Fig. 8, although significantly different from a flat line,

Downloaded from https://academic.oup.com/mnras/article-abstract/495/4/3881/5838753 by The Open University user on 22 June 2020

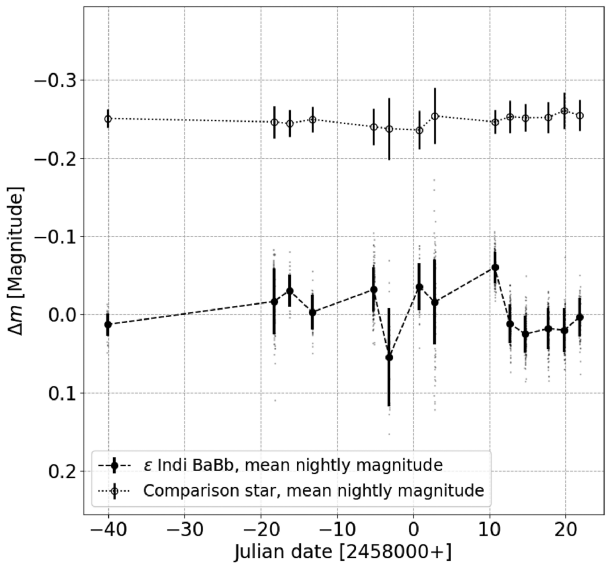

Figure 9. Zero-point corrected differential photometry for the entire observing campaign for the target. Individual differential magnitudes are shown as faint dots, and the mean magnitude for both the target (filled circles) and red comparison star (hollow circles) are plotted as the large markers, with associated error bars. These error bars are the root sum of squares of the standard deviation of the photometry on each night and the error associated with the photometric zero-point shift.

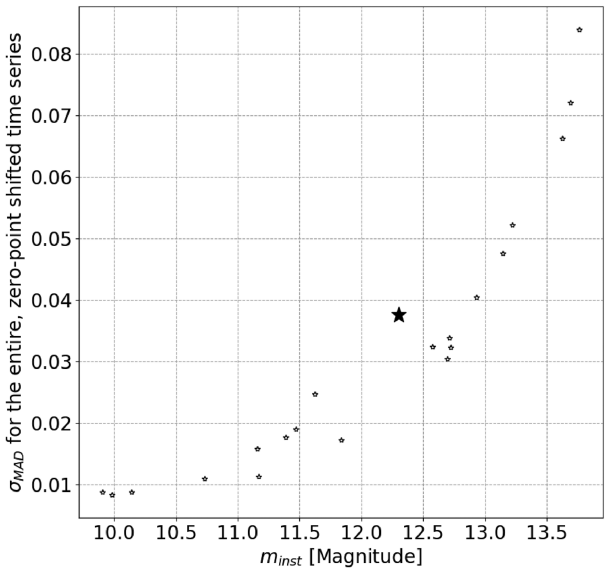

Figure 10. The median absolute deviation – scaled to a standard deviation – of the entire zero-point shifted times series versus instrumental magnitude for stars (small hollow stars) near the target (large filled black star) on the chip.

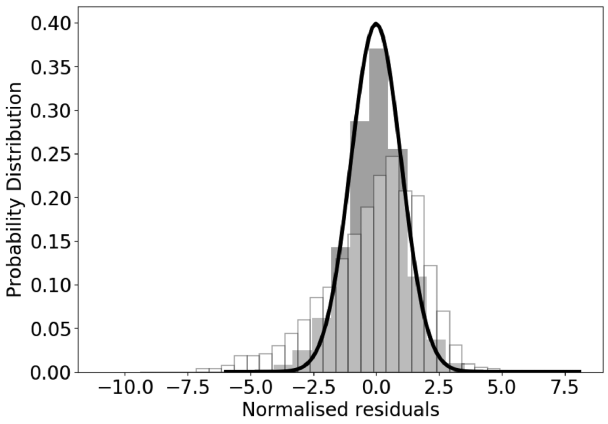

Figure 11. Normalized histograms for the normalized residuals of the target (white) and neighbouring stars, binned collectively into an empirical distribution (grey). A unit Gaussian is overlain for comparison, and shows clear similarities with the empirical distribution. This contrasts with the target's histogram, which is statistically significantly different than the empirical distribution (p-value from KS test is 3.1×10^{-24}) and shows clear asymmetry.

the relative error is very large, and the gradient itself is far lower than the level of variation we claim to see on this night-to-night time-scale. This suggests that the mean brightness of the target is not a strong function of either seeing or airmass.

Given that there were changes in pointing over the 2 months of observing, it is necessary to include some assessment of any consequent systematic impact on the night-to-night time series. It is expected that this effect, if present, should be similar for neighbouring stars on the chip. For this reason, the quantitative assessment of night-to-night variability which follows is done with reference to the time series of stars neighbouring the target. Specifically, we select stars that are within a 6 × 6 arcmin box centred on the target.

We plot the instrumental magnitude against the $\sigma_{\rm MAD}$ of the entire zero-point-corrected ∼2 month time series in Fig. 10 for the target (large filled black star) and its nearest neighbours (small hollow stars). Certainly, this suggests enhanced variability in the target over the 2 months. To quantify how the time series in Fig. 9 differs from the simple model of a straight line (with Gaussian measurement noise), one can generate a histogram of the normalized residuals relative to the mean magnitude level, $\overline{m}_{\rm inst}$, which for any magnitude measurement $m_{{\rm inst},\,n}$ with uncertainty σ_n is

$$R_n = \frac{m_{{\rm inst},n} - \overline{m}_{\rm inst}}{\sigma_n}, \tag{4}$$

and compare the normalized histogram – such that the counts integrate to 1 – against a Gaussian with mean 0 and variance 1. A Kolmogorov–Smirnoff test can then be used to compare the similarity of the two distributions (Massey Jr 1951). Given that systematics in the photometry could introduce non-Gaussian noise into the night-to-night time series, a better approach is to compare the normalized residuals of the target time series against an *empirical* distribution. To construct this, we generate a histogram of the normalized residuals of the neighbouring stars – the same as in Fig. 10 – and perform a KS test between this empirical distribution and that of the target. This gives us a quantitative measure of how different the target's night-to-night variation is from the neighbouring stars. We show this in Fig. 11, where the target's distribution (white histogram) is overlain on to this empirical distribution (grey). By-eye inspection shows clear differences between the two distributions – note, for example, the asymmetry in the target's histogram – and the returned p-value from a KS test is very low, at 3.1×10^{-24}. A unit Gaussian is overlain for comparison, which, as expected, shows similarities with the empirical distribution, but clearly deviates from the target's.

Downloaded from https://academic.oup.com/mnras/article-abstract/495/4/3881/5838753 by The Open University user on 22 June 2020

4 DISCUSSION

4.1 No photometric period

The rotation periods of ϵ Indi Ba and Bb are not known. Provided the photometric signatures of the rotation periods of each of the brown dwarfs exceed the levels of variation associated with evolving weather systems or flaring (and of course, the inherent white noise), one might expect to see a superposition of two distinct periods. In reality, we expect the T1 component to dominate any photometric signal, due both to its greater brightness, and presumably greater cloud coverage given its evolutionary proximity to the L/T transition. Indeed, from the resolved *I*-band photometry in Table 1, the T6 component only contributes 20 per cent of the total *I*-band flux. If all the measured variations were associated with this fainter component, it would have to be implausibly variable – by more than 50 per cent – to reproduce the variation we see.

Neither a Lomb–Scargle periodogram (Scargle 1982) nor auto-correlation function analysis applied to the individual nightly time series returned a consistent period. A flexible Gaussian Process model described by a periodic kernel was conditioned on the entire data set (Foreman-Mackey et al. 2017). The marginal posterior distribution of the period parameter was sampled with a Markov chain Monte Carlo method, and this too failed to reveal any convincing periodicity.

4.2 No evidence for lightning

4.2.1 A test for asymmetry in the within-night time series

Following Cody et al. (2014), for each night of *I*-band observations, we define the metric *M*, such that

$$M = (\langle d_{10\,\mathrm{percent}} \rangle - d_{\mathrm{med}})/\sigma_d, \quad (5)$$

where $\langle d_{10\ \mathrm{per\ cent}} \rangle$ is the mean of the 10 per cent highest and lowest magnitude values of the time series, and d_{med} and σ_d are the median flux level and rms scatter for the entire nightly time series, respectively. In all other time series analyses presented in this work (i.e. the period search, monitoring of the long-term changes in mean brightness, etc.), a 4σ clip was used for the differential photometry. In this section only – which describes an analysis specifically designed to probe for possible lightning strikes – we slightly relax this constraint, and instead clip 5σ outliers from the within-night differential photometry. This was done to continue to guard against both spurious photometry and cosmic ray hits, but also allow for potentially large spikes in brightness.

Application of equation (5) to each of the individual nightly ϵ Indi Ba and Bb time series revealed no consistent asymmetry above the median flux level. For lightning-like signatures (i.e. a stochastic brightening above the median flux level), one would expect to recover negative values of *M*. Rather, both positive and negative values for *M* were found, randomly distributed, with a mean and median of 0.025 and −0.043 (see Fig. 12). The largest absolute values of *M* were seen to correspond to nights with occasional 'blips' above or below the median flux level, or more rarely, on nights with a smooth, weakly underlying trend (e.g. 2017 August 28). The 'blips' in the target's time series are also seen on occasion in the comparison stars' within-night time series, producing similar values of *M*, which suggests imperfections with the photometry, and not any real variation. Indeed, the *M* values for the red comparison star whose time series are shown alongside the target in Fig. 3 are also plotted, and show a similar spread in *M* values, albeit at a somewhat lower amplitude. The sensitivity of the *M* metric to these systematic 'blips' in an otherwise quiet time series is not surprising, as its value will be strongly influenced by these few, outlying points. Indeed, in contrast to the time series analysed here, Cody et al. (2014) apply this metric to time series of clearly variable sources, where the level of true astrophysical variation greatly exceeds the noise.

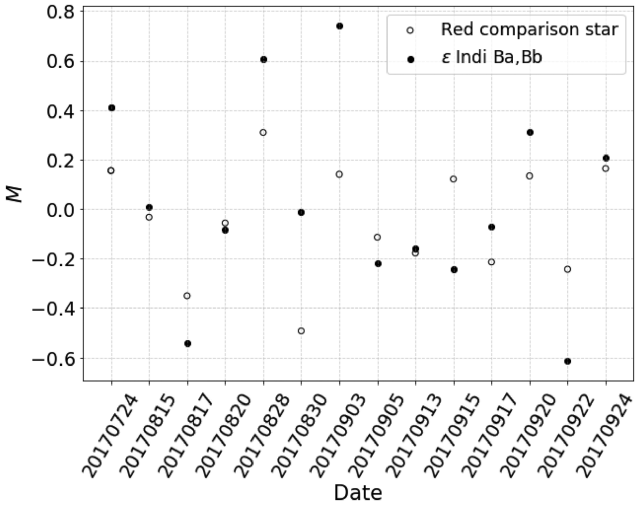

Figure 12. Values for the metric described by equation (5) on each night, for both the target (filled circles) and a red comparison star (hollow circles).

4.2.2 Implications for the properties of extrasolar lightning

One could consider what upper limits these non-detections for lightning – both in the *I*-band time series and the *V* and Hα images – place on the physical properties of the strikes in the atmospheres of brown dwarfs. However, the physical parameters that describe the properties of lightning in extrasolar environments remain difficult to constrain given our non-detections. These include the power and duration of strikes, their flash density (i.e. the rate of strikes per unit area), percentage coverage of strikes over the brown dwarf's hemisphere, and how the power is radiated into frequencies across the optical (see e.g. Bailey et al. 2014; Hodosán et al. 2016). Consequently, all we can confidently say is that (1) if lightning strikes on ϵ Indi Ba and Bb are indeed observable above the noise in our *I*-band time series (with a median $\sigma_{\mathrm{MAD}} = 23$ mmag) we do not observe any strikes in a total ∼42 h of coverage. That is, the rate of lightning strikes that emerge out of the atmosphere is <0.02 strikes per hour. (2) We do not see anything like the increase in brightness estimated from the most promising *combination* of parameters detailed in Hodosán (2017).

4.3 Days-long variability

The lack of any clear periodicity and significant days-long variability could suggest we are viewing the system close to a pole. The large changes in mean brightness suggest inhomogeneity of surface features on the brighter T1 component. Given the extreme coolness of the target (see Table 1), these almost certainly arise from large-scale changes in the cloud coverage. By large scale, we simply mean that the cause of the variation is not localized to any single part of the surface, i.e. the variation is caused by some net effect due to the changing cloud configurations expected to cover this ultracool target. The lack of any other clear signal can be viewed as

Downloaded from https://academic.oup.com/mnras/article-abstract/495/4/3881/5838753 by The Open University user on 22 June 2020

beneficial, in that we measure the 'pure' signal associated with these inhomogeneities only, free from any rotational influence. Although cloud coverage is the most likely explanation for the variability, we note that the plausibility of any particular scenario will be dependent on spectroscopic follow-up of this and other objects, in addition to numerous theoretical assessments.

If large-scale changes in the cloud coverage are responsible for changes in mean brightness – which is active on time-scales as short as 2 d – these clouds might occur with a banded structure similar to the striking clouds seen in Jupiter's atmosphere (Apai et al. 2017). The regions of cyclonic shear at the boundaries between these bands are a perfect environment for generating lightning, as seen for Jupiter and Saturn in our own Solar system (Little et al. 1999). Our current inability to put tight prior constraints on the expected properties of lightning makes planning searches designed to probe these signatures far from straightforward.

Certainly, this work suggests that conventional CCD imaging in either narrow or broad-band filters is not an ideal strategy to detect such signatures, even at a fairly high cadence. Given the expected sub-second duration of any individual lightning strike, the shorter the exposure time, the more easily detectable a given strike will be above the background flux of the hosting source. Technological advances with high-frame rate cameras – which make use of special low-light-level detectors (e.g. electron-multiplying CCDs, and more recently, CMOS Imaging Sensors) – have extended time domain astronomy to this sub-second regime. The simultaneous multiwavelength, high-cadence studies made possible by attaching these devices to medium- to large-sized telescopes [e.g. the recent OPTICAM instrument (Castro et al. 2019)] may provide the crucial observational requirements.

5 CONCLUSIONS

We have discussed the results of an analysis of 14 nights of *I*-band photometric monitoring of the nearby ϵ Indi Ba and Bb brown dwarf binary. The target typically appears to be unremarkably quiet on the hour-long time-scales of each night of observing, which contrasts with the large changes in mean brightness – by as much as 0.10 mag – which we measure between nights across the entire 2 month campaign. The hours-long time-scale stability of the target, and lack of any clear periodicity, suggests that the large changes in mean brightness may arise from changes in the large-scale cloud structure. The regular nightly visits to this target and overall long-term coverage of this data set provide a new insight into the irregular, days-long variability exhibited by brown dwarfs at the L/T transition. Indeed, we expect that this signal is associated with ϵ Indi Ba, which is both the brighter of the two components, and of spectral type T1, and so likely far cloudier than its cooler T6 companion.

Lightning will very likely occur where dynamic clouds form, and complementary *V*-band and Hα images were acquired to search for stochastic signatures diagnostic of the lightning strikes assumed to be present in the atmospheres of these brown dwarfs. No $>3\sigma$ detections above the background at the position of the target were found in these passbands, nor is there any suggestion of short-time-scale, asymmetric 'flickering' in the *I*-band time series. The necessarily long exposures required for conventional CCDs – such that the signal of interest exceeds the readout noise – limit our ability to detect these short-time-scale events. Exploration of the sub-second time variability of astrophysical sources is being made increasingly feasible with technological advances of high-frame-rate detectors, and we recommend future lightning hunters adopt these new technologies for their searches.

ACKNOWLEDGEMENTS

We extend a collective thank you to the MiNDSTEp consortium – both the observers and those responsible for the smooth running of operations – for adopting this side project for the 2017 observing season. LM acknowledges support from the University of Rome Tor Vergata through 'Mission: Sustainability 2017' fund. ChH and GH gratefully acknowledge the support of the European Research Council (ERC) Starting Grant no. 257431.

REFERENCES

Apai D. et al., 2017, Science, 357, 683
Apai D. et al., 2019, BAAS, 51, id. 204
Artigau É., Bouchard S., Doyon R., Lafrenière D., 2009, ApJ, 701, 1534
Bailey R., Helling C., Hodosán G., Bilger C., Stark C. R., 2014, ApJ, 784, 43
Bertin E., Arnouts S., 1996, A&AS, 117, 393
Bessell M., 1990, PASP, 102, 1181
Bessell M., Castelli F., Plez B., 1998, A&A, 333, 231
Biller B. A. et al., 2018, AJ, 155, 95
Burrows A., Sudarsky D., Hubeny I., 2006, ApJ, 640, 1063
Castro A. et al., 2019, Revista Mexicana de Astronomía y Astrofísica, 55, 363
Cody A. M. et al., 2014, AJ, 147, 82
Curran P. A., 2014, preprint (arXiv:1411.3816)
Eriksson S. C., Janson M., Calissendorff P., 2019, A&A, 629, A145
Foreman-Mackey D., Agol E., Ambikasaran S., Angus R., 2017, AJ, 154, 220
Helling C. et al., 2008, MNRAS, 391, 1854
Helling C. et al., 2016, Surv. Geophys., 37, 705
Hodosán G., 2017, PhD thesis, Univ. St Andrews
Hodosán G., Rimmer P. B., Helling C., 2016, MNRAS, 461, 1222
King R. R., McCaughrean M. J., Homeier D., Allard F., Scholz R.-D., Lodieu N., 2010, A&A, 510, A99
Knapp G. et al., 2004, AJ, 127, 3553
Koen C., 2003, MNRAS, 346, 473
Koen C., 2005, MNRAS, 360, 1132
Koen C., 2009, MNRAS, 395, 531
Koen C., 2012, MNRAS, 428, 2824
Koen C., Matsunaga N., Menzies J., 2004, MNRAS, 354, 466
Koen C., Tanabé T., Tamura M., Kusakabe N., 2005, MNRAS, 362, 727
Little B. et al., 1999, Icarus, 142, 306
McCaughrean M., Close L. M., Scholz R.-D., Lenzen R., Biller B., Brandner W., Hartung M., Lodieu N., 2004, A&A, 413, 1029
Massey F. J., Jr, 1951, J. Am. Stat. Assoc., 46, 68
Metchev S. A. et al., 2015, ApJ, 799, 154
Prusti T. et al., 2016, A&A, 595, A1
Radigan J., Lafrenière D., Jayawardhana R., Artigau E., 2014, ApJ, 793, 75
Scargle J. D., 1982, ApJ, 263, 835
Scholz A., Eislöffel J., 2004, A&A, 419, 249
Scholz R.-D., McCaughrean M. J., Lodieu N., Kuhlbrodt B., 2003, A&A, 398, L29
Volland H., 2013, Atmospheric Electrodynamics, Vol. 11. Springer Sci. Bus. Media, Heidelberg
Vos J. M. et al., 2019, MNRAS, 483, 480
Yang H. et al., 2016, ApJ, 826, 8
Zarka P., Farrell W., Kaiser M., Blanc E., Kurth W., 2004, Planet. Space Sci., 52, 1435
Brown et al., 2018, A&A, 616, A1

SUPPORTING INFORMATION

Supplementary data are available at *MNRAS* online.

Table_of_Target_and_Comparisons_Instrumental_Magnitudes.csv

Please note: Oxford University Press is not responsible for the content or functionality of any supporting materials supplied by

Downloaded from https://academic.oup.com/mnras/article-abstract/495/4/3881/5838753 by The Open University user on 22 June 2020

the authors. Any queries (other than missing material) should be directed to the corresponding author for the article.

APPENDIX A: SUPPLEMENTARY TIME SERIES

The normalized differential photometry for the remaining nine nights that are not shown in Section 3 is plotted in Figs A1 and A2.

The *I*-band differential photometry for all nights is publicly available for download in a machine-readable form via ScholarOne. We include the target time series, and those of the 16-large comparison star ensemble to allow independent validation of the night-to-night zero-point calculations. These instrumental magnitudes have not been transformed to a standard photometric system, and are set on an arbitrary scale. The first five rows are shown in Table A1.

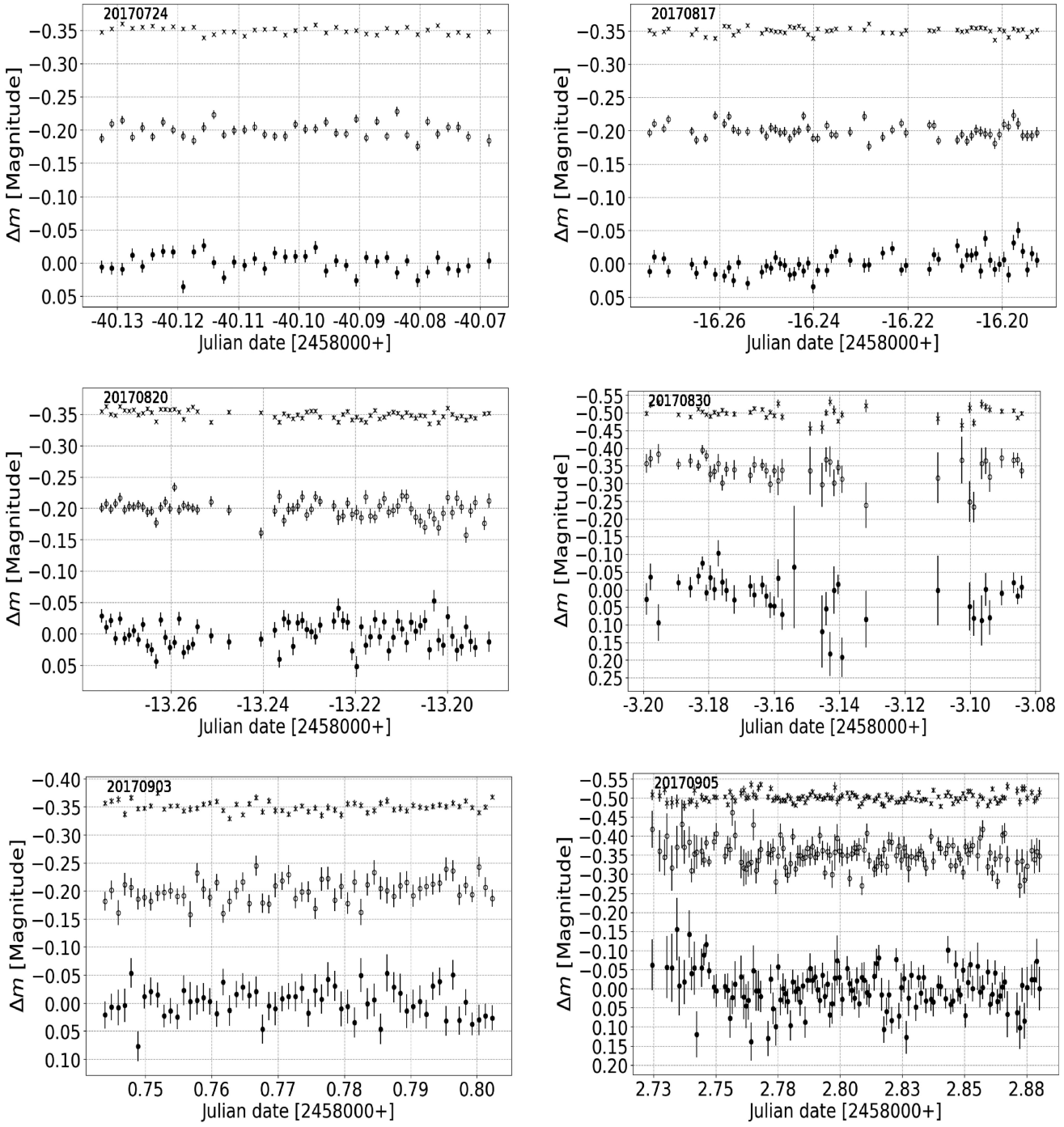

Figure A1. Normalized differential photometry, as in Fig. 3, for six additional nights not shown in Section 3. As noted in Section 2, observations on the night of 2017 August 30 were interrupted by passing clouds.

Downloaded from https://academic.oup.com/mnras/article-abstract/495/4/3881/5838753 by The Open University user on 22 June 2020

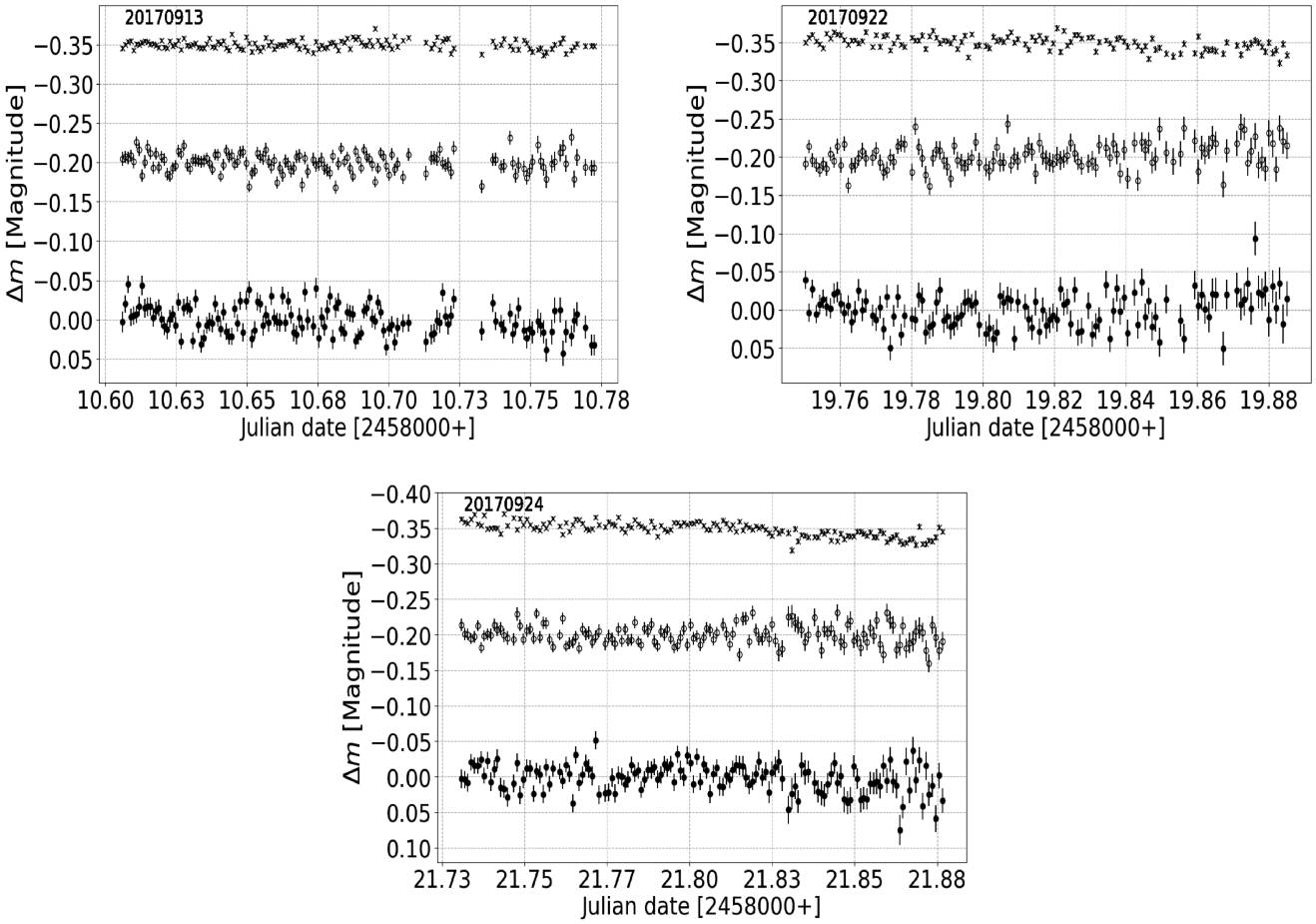

Figure A2. Normalized differential photometry, as in Fig. 3, for three additional nights not shown in Section 3.

Table A1. An extract of the first five rows of the table hosting the *I*-band differential photometry used in this work for the target and comparison stars. These instrumental magnitudes have not been transformed to a standard photometric system, and are set on an arbitrary scale. Here, the photometry measured on different nights has not been zero-point corrected. The full table is available in a machine-readable form online.

ϵ Indi Ba and Bb JD (245 8000+)	$m_{\rm inst}$	$m_{\rm err}$	Comparison1 JD (245 8000+)	$m_{\rm inst}$	$m_{\rm err}$	...	Comparison16 JD (245 8000+)	$m_{\rm inst}$	$m_{\rm err}$
−40.1326	12.3171	0.0090	−40.1326	11.5945	0.0073	...	−40.1326	11.3186	0.0069
−40.1309	12.3193	0.0097	−40.1309	11.6133	0.0077	...	−40.1309	11.3411	0.0071
−40.1292	12.3207	0.0093	−40.1292	11.6081	0.0075	...	−40.1292	11.3319	0.0072
−40.1275	12.2992	0.0097	−40.1275	11.6029	0.0080	...	−40.1275	11.3228	0.0075
−40.1258	12.3165	0.0093	−40.1258	11.6110	0.0073	...	−40.1258	11.3291	0.0069
...	...	...	...	...	...	...	...	...	...

APPENDIX B: SUPPLEMENTARY CORRELATION PLOTS

See below Figs B1-B5 for the remaining correlation plots not shown in the main text of the paper.

Table B1. Table showing the Spearman correlation coefficient (SCC) and best-fitting slope for the photometry against airmass over several nights for the target and a comparison star.

Date	Star	Slope (versus airmass)	SCC (versus airmass)
2017-07-24	Red comparison star	0.007 ± 0.028	$0.05^{+0.18}_{-0.19}$
	ϵ Indi Ba and Bb	0.034 ± 0.030	$0.14^{+0.19}_{-0.18}$
2017-08-15	Red comparison star	0.137 ± 0.122	$0.04^{+0.14}_{-0.14}$
	ϵ Indi Ba and Bb	0.588 ± 0.054	$0.65^{+0.07}_{-0.08}$

Downloaded from https://academic.oup.com/mnras/article-abstract/495/4/3881/5838753 by The Open University user on 22 June 2020

Table B1 – *continued*

Date	Star	Slope (versus airmass)	SCC (versus airmass)
2017-08-17	Red comparison star	0.056 ± 0.039	$0.13^{+0.15}_{-0.16}$
	ϵ Indi Ba and Bb	−0.193 ± 0.050	$-0.37^{+0.15}_{-0.12}$
2017-08-20	Red comparison star	0.062 ± 0.036	$0.16^{+0.14}_{-0.14}$
	ϵ Indi Ba and Bb	−0.011 ± 0.058	$0.03^{+0.14}_{-0.14}$
2017-08-30	Red comparison star	0.010 ± 0.021	$0.17^{+0.21}_{-0.20}$
	ϵ Indi Ba and Bb	0.044 ± 0.030	$0.28^{+0.16}_{-0.18}$
2017-09-03	Red comparison star	−0.100 ± 0.040	$-0.25^{+0.15}_{-0.13}$
	ϵ Indi Ba and Bb	0.046 ± 0.065	$0.02^{+0.17}_{-0.16}$
2017-09-05	Red comparison star	0.012 ± 0.015	$0.11^{+0.11}_{-0.12}$
	ϵ Indi Ba and Bb	0.027 ± 0.023	$0.09^{+0.12}_{-0.11}$
2017-09-13	Red comparison star	0.009 ± 0.015	$0.04^{+0.12}_{-0.10}$
	ϵ Indi Ba and Bb	0.075 ± 0.020	$0.18^{+0.13}_{-0.08}$
2017-09-15	Red comparison star	−0.036 ± 0.013	$-0.20^{+0.09}_{-0.08}$
	ϵ Indi Ba and Bb	0.061 ± 0.016	$0.22^{+0.08}_{-0.09}$
2017-09-17	Red comparison star	−0.006 ± 0.011	$0.00^{+0.11}_{-0.13}$
	ϵ Indi Ba and Bb	−0.033 ± 0.017	$-0.11^{+0.10}_{-0.09}$
2017-09-20	Red comparison star	−0.015 ± 0.010	$-0.07^{+0.08}_{-0.09}$
	ϵ Indi Ba and Bb	0.074 ± 0.017	$0.21^{+0.12}_{-0.09}$
2017-09-22	Red comparison star	−0.012 ± 0.003	$-0.26^{+0.12}_{-0.05}$
	ϵ Indi Ba and Bb	−0.006 ± 0.005	$-0.09^{+0.11}_{-0.11}$
2017-09-24	Red comparison star	0.002 ± 0.003	$0.07^{+0.14}_{-0.14}$
	ϵ Indi Ba and Bb	0.012 ± 0.004	$0.19^{+0.12}_{-0.11}$

Table B2. Table showing the Spearman correlation coefficient (SCC) and best-fitting slope for the photometry against FWHM (as a proxy for seeing) over several nights for the target and a comparison star.

Date	Star	Slope (versus FWHM)	SCC (versus FWHM)
2017-07-24	Red comparison star	0.005 ± 0.009	$0.06^{+0.20}_{-0.19}$
	ϵ Indi Ba and Bb	−0.008 ± 0.011	$-0.11^{+0.20}_{-0.17}$
2017-08-15	Red comparison star	0.006 ± 0.003	$0.16^{+0.12}_{-0.13}$
	ϵ Indi Ba and Bb	0.047 ± 0.007	$0.64^{+0.08}_{-0.09}$
2017-08-17	Red comparison star	0.007 ± 0.009	$0.05^{+0.16}_{-0.18}$
	ϵ Indi Ba and Bb	−0.028 ± 0.013	$-0.20^{+0.17}_{-0.15}$
2017-08-20	Red comparison star	0.009 ± 0.004	$0.25^{+0.12}_{-0.14}$
	ϵ Indi Ba and Bb	0.001 ± 0.006	$0.01^{+0.14}_{-0.14}$
2017-08-30	Red comparison star	0.000 ± 0.020	$0.03^{+0.21}_{-0.20}$
	ϵ Indi Ba and Bb	0.037 ± 0.024	$0.14^{+0.17}_{-0.19}$
2017-09-03	Red comparison star	−0.002 ± 0.004	$-0.06^{+0.18}_{-0.15}$
	ϵ Indi Ba and Bb	−0.009 ± 0.005	$-0.13^{+0.17}_{-0.15}$
2017-09-05	Red comparison star	−0.006 ± 0.010	$0.06^{+0.11}_{-0.11}$
	ϵ Indi Ba and Bb	−0.006 ± 0.010	$0.06^{+0.11}_{-0.10}$
2017-09-13	Red comparison star	0.004 ± 0.003	$0.09^{+0.04}_{-0.06}$
	ϵ Indi Ba and Bb	0.014 ± 0.004	$0.18^{+0.09}_{-0.10}$
2017-09-15	Red comparison star	0.005 ± 0.003	$0.10^{+0.08}_{-0.09}$
	ϵ Indi Ba and Bb	0.007 ± 0.004	$0.08^{+0.09}_{-0.09}$
2017-09-17	Red comparison star	0.002 ± 0.004	$0.02^{+0.08}_{-0.05}$
	ϵ Indi Ba and Bb	0.000 ± 0.005	$0.01^{+0.10}_{-0.07}$
2017-09-20	Red comparison star	−0.001 ± 0.002	$-0.01^{+0.09}_{-0.09}$
	ϵ Indi Ba and Bb	0.017 ± 0.003	$0.38^{+0.07}_{-0.07}$
2017-09-22	Red comparison star	−0.009 ± 0.004	$-0.15^{+0.09}_{-0.15}$
	ϵ Indi Ba and Bb	0.002 ± 0.006	$0.04^{+0.11}_{-0.11}$
2017-09-24	Red comparison star	0.000 ± 0.002	$0.01^{+0.08}_{-0.08}$
	ϵ Indi Ba and Bb	0.012 ± 0.003	$0.28^{+0.10}_{-0.11}$

Downloaded from https://academic.oup.com/mnras/article-abstract/495/4/3881/5838753 by The Open University user on 22 June 2020

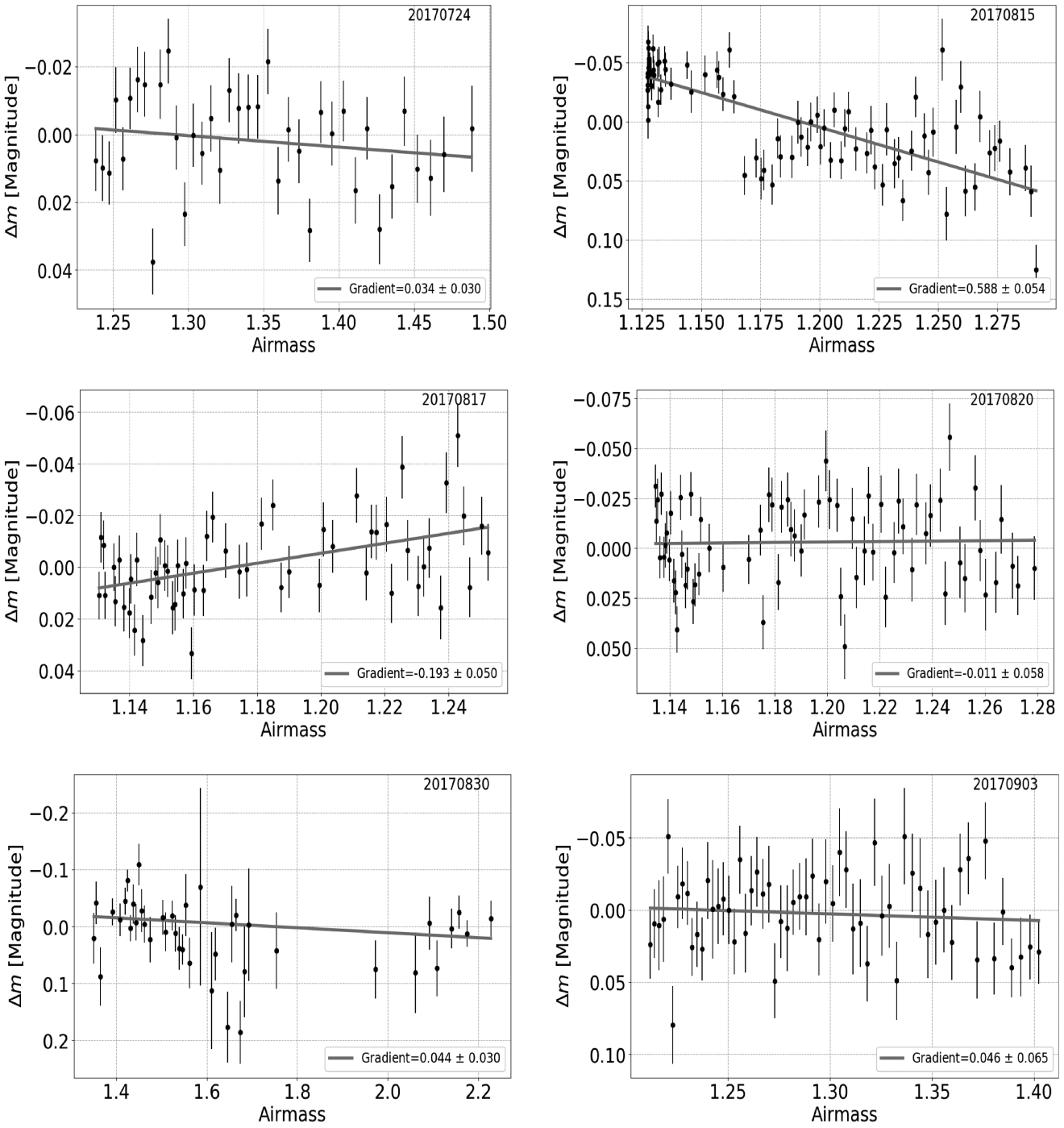

Figure B1. Normalized differential photometry versus airmass for six additional nights not shown in Section 3.1 (2017 July 24 to 2017 September 3). The gradient and corresponding bootstrap uncertainty of the plotted best-fitting straight lines, and the Pearson Correlation coefficients, are shown in the legends.

Downloaded from https://academic.oup.com/mnras/article-abstract/495/4/3881/5838753 by The Open University user on 22 June 2020

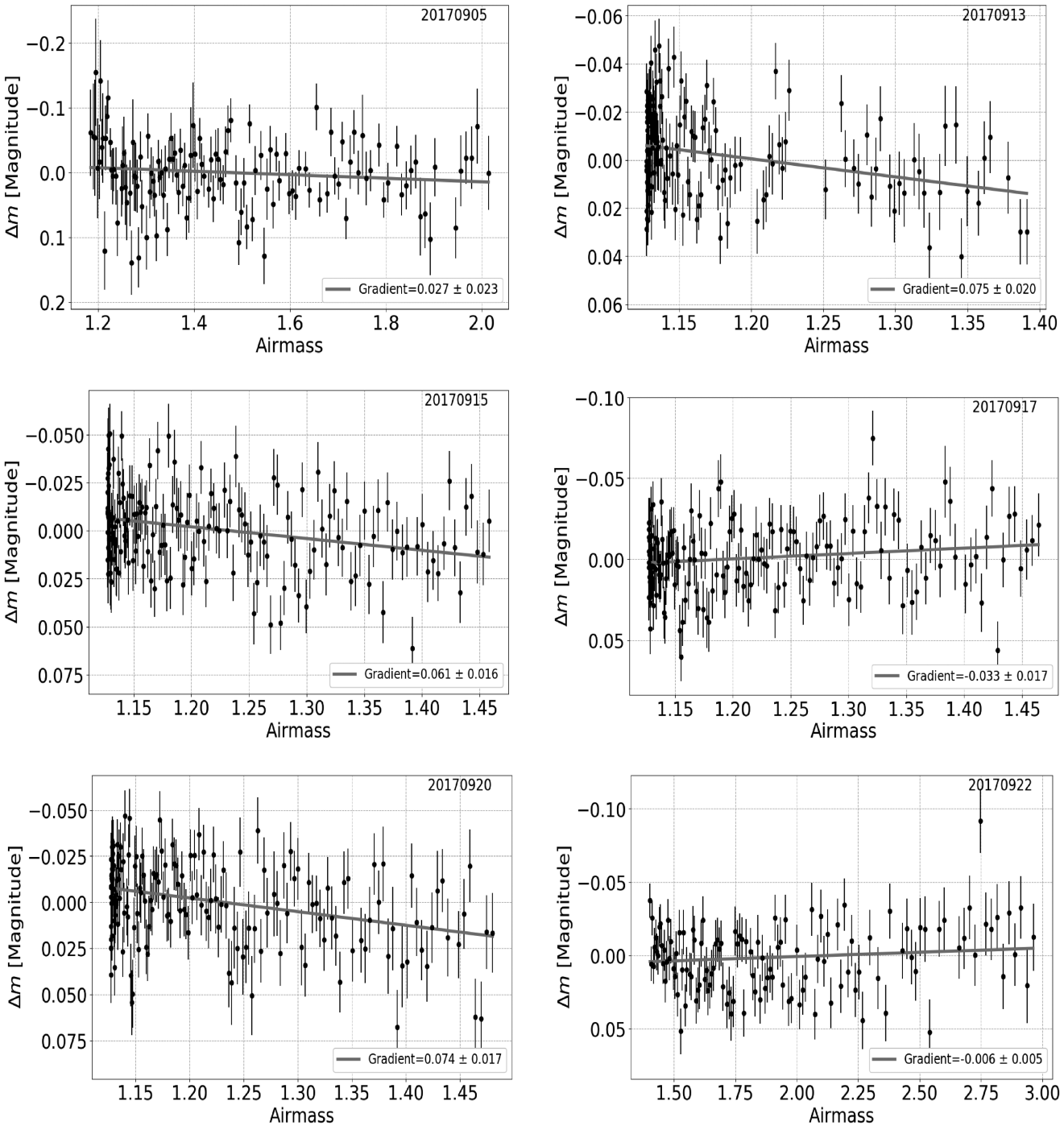

Figure B2. Normalized differential photometry versus airmass for six additional nights not shown in Section 3.1 (2017 September 5 to 22). The gradient and corresponding bootstrap uncertainty of the plotted best-fitting straight lines, and the Pearson Correlation coefficients, are shown in the legends.

Downloaded from https://academic.oup.com/mnras/article-abstract/495/4/3881/5838753 by The Open University user on 22 June 2020

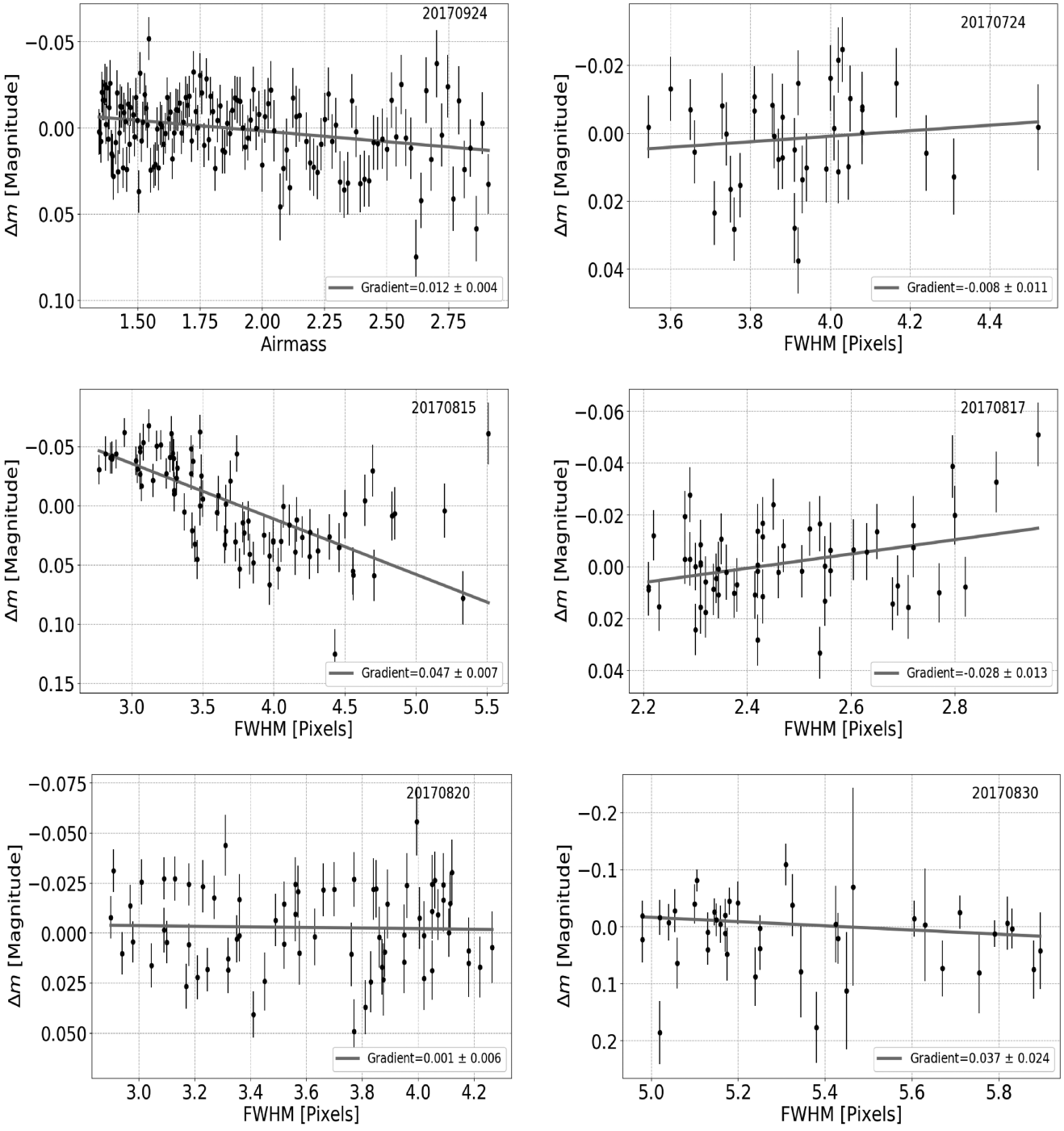

Figure B3. (Top left) Normalized differential photometry versus airmass for the night of 2017 September 24. (Rest) Normalized differential photometry versus image FWHM (as a proxy for seeing) for five additional nights not shown in Section 3.1 (2017 July 24 to 2017 August 30). The gradient and corresponding bootstrap uncertainty of the plotted best-fitting straight lines, and the Pearson Correlation coefficients, are shown in the legends.

Downloaded from https://academic.oup.com/mnras/article-abstract/495/4/3881/5838753 by The Open University user on 22 June 2020

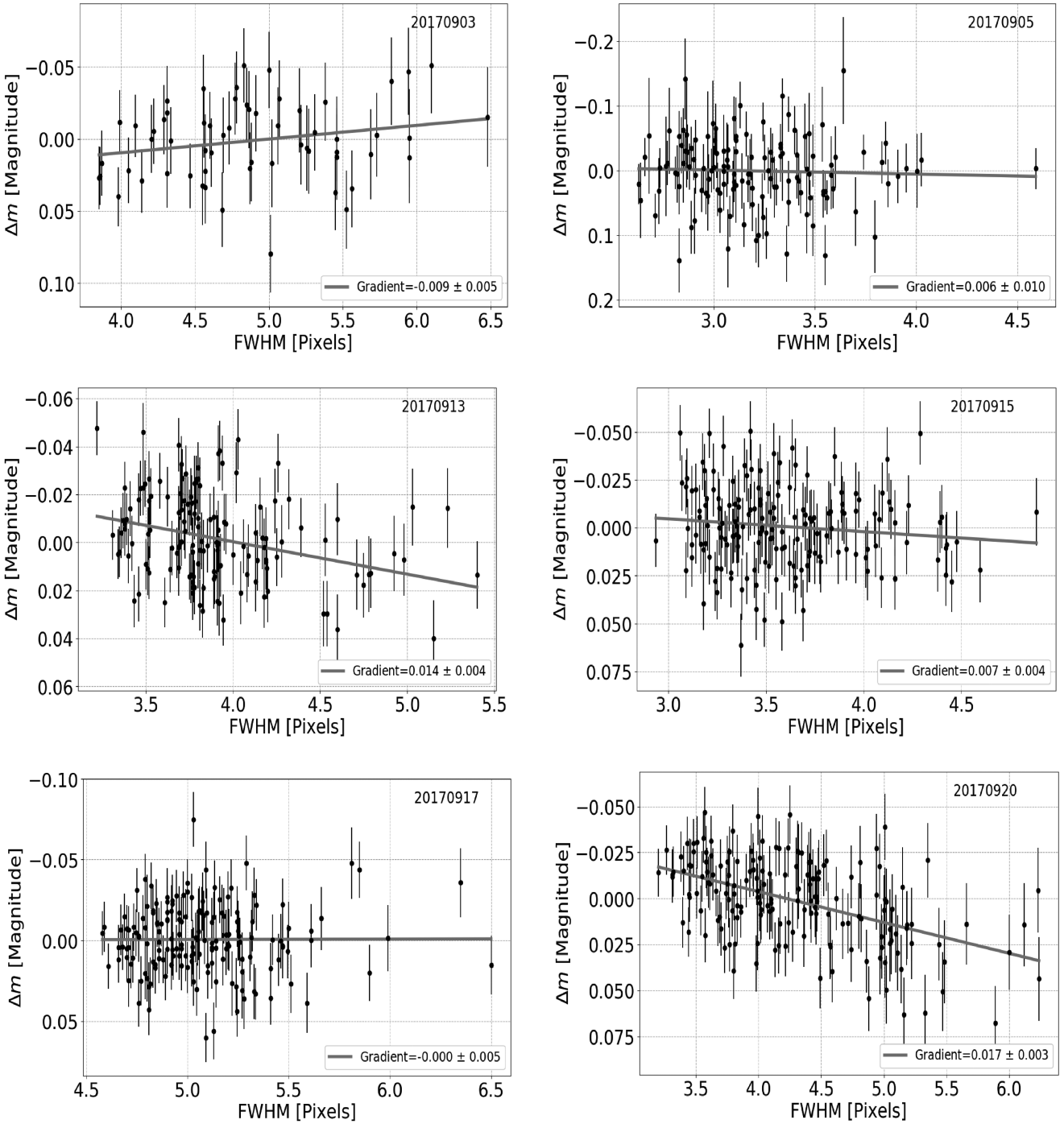

Figure B4. Normalized differential photometry versus image FWHM (as a proxy for seeing) for six additional nights not shown in Section 3.1 (2017 September 3 to 20). The gradient and corresponding bootstrap uncertainty of the plotted best-fitting straight lines, and the Pearson Correlation coefficients, are shown in the legends.

Downloaded from https://academic.oup.com/mnras/article-abstract/495/4/3881/5838753 by The Open University user on 22 June 2020

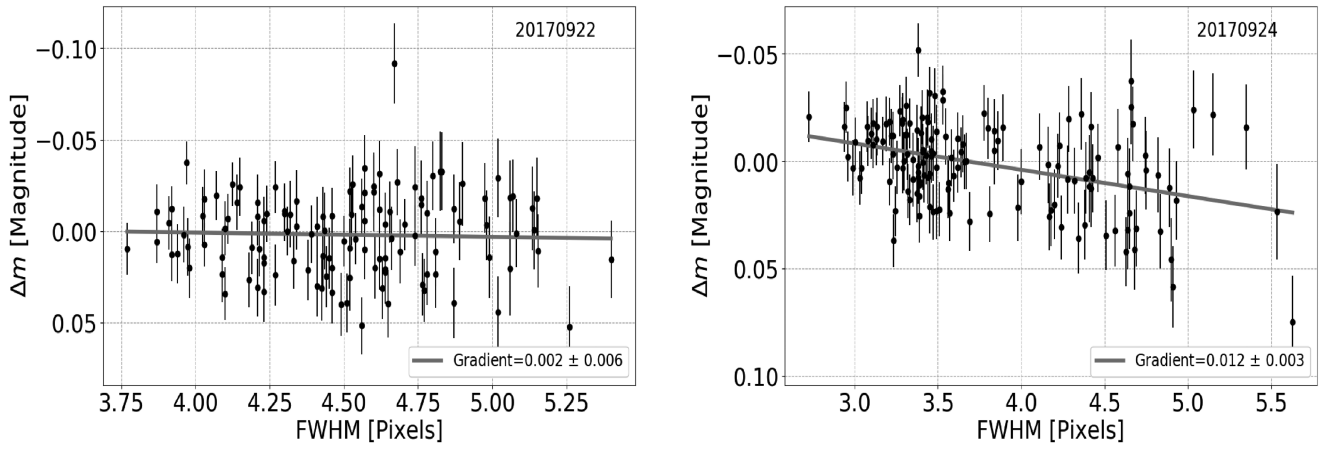

Figure B5. Normalized differential photometry versus image FWHM (as a proxy for seeing) for two additional nights not shown in Section 3.1 (2017 September 22 to 24). The gradient and corresponding bootstrap uncertainty of the plotted best-fitting straight lines, and the Pearson Correlation coefficients, are shown in the legends.

APPENDIX C: THE OBSERVABLE SIGNAL STRENGTH OF LIGHTNING FLASHES

In equations (C1) and (C2) below, all fluxes, I, are in units of Jansky (Jy) – where 1 W.s.m^{-2} $= 10^{26}$ Jy – and all other variables are in SI.

Following Hodosán (2017), the total observable flux from a lightning storm on the surface of a brown dwarf may be expressed as

$$I_{\rm obs} = I_{\rm opt,fl}\frac{\tau_{\rm fl}}{\tau_{\rm obs}}n_{\rm tot,\,fl}, \tag{C1}$$

where $I_{\rm opt,\,fl}$ is the optical flux from a single strike, $\tau_{\rm fl}$ is the duration of the strike, $\tau_{\rm obs}$ is the exposure time, and $n_{\rm tot,\,fl}$ is the total number of observed flashes. Next, we can write $I_{\rm opt,\,fl}$ as

$$I_{\rm opt,fl} = \frac{P_{\rm opt,fl}}{f_{\rm eff}}\frac{10^{26}}{4\pi d^2}, \tag{C2}$$

when observing in a filter with an effective frequency of $f_{\rm eff}$, for a flash with an optical power of $P_{\rm opt,\,fl}$ at a distance of d. Finally, the total number of flashes over the visible hemisphere of the brown dwarf can be written as

$$n_{\rm tot,\,fl} = \rho_{\rm fl} \times 2\pi R^2 \times \tau_{\rm obs} \tag{C3}$$

for a flash density of $\rho_{\rm fl}$, and a radius of R, which is assumed to be $1R_{\rm Jupiter}$. Subsequently, any estimated fluxes can be converted to magnitudes via Pogson's formula,

$$m - m_{\rm zp} = -2.5\log\frac{F}{F_{\rm zp}}, \tag{C4}$$

where the relevant magnitude and flux zero-points (i.e. $m_{\rm zp}$ and $F_{\rm zp}$) for the Johnson-Cousin filters used in this work are taken from Bessell (1990) and Bessell, Castelli & Plez (1998), respectively. We again refer the reader to Hodosán (2017) for full details of the parameters – both instrumental and physical – used in this work.

Substituting equation (C3) into equation (C1) shows that the exposure times cancel, and so $I_{\rm obs}$ only depends on the duration of the lightning discharge. This at first seems strange, but note that here we are not trying to detect a *single* strike during an otherwise flat time series – where a short exposure time really would be of benefit – but rather this is simply a measure of any net brightening of the source due to the presence of a lightning storm, i.e. very many strikes occurring collectively, with a rate per unit area described by the flash density, during any given exposure.

[1]*Centre for Exoplanet Science, University of St Andrews, North Haugh KY16 9SS, UK*
[2]*SUPA, School of Physics and Astronomy, University of St Andrews, North Haugh KY16 9SS, UK*
[3]*SRON Netherlands Institute for Space Research, Sorbonnelaan 2, NL-3584 CA Utrecht, the Netherlands*
[4]*Astronomisches Rechen-Institut, Zentrum für Astronomie der Universität Heidelberg (ZAH), D-69120 Heidelberg, Germany*
[5]*Niels Bohr Institute and Centre for Star and Planet Formation, University of Copenhagen, Øster Voldgade 5, DK-1350 Copenhagen, Denmark*
[6]*Unidad de Astronomía, Universidad de Antofagasta, Av. Angamos 601, Antofagasta, Chile*
[7]*Department of Physics, Isfahan University of Technology, Isfahan 84156-83111, Iran*
[8]*Centre for Electronic Imaging, Department of Physical Sciences, The Open University, Milton Keynes MK7 6AA, UK*
[9]*Institute for Astronomy, University of Edinburgh, Royal Observatory, Edinburgh EH9 3HJ, UK*
[10]*Dipartimento di Fisica 'E.R. Caianiello', Università di Salerno, Via Giovanni Paolo II 132, I-84084 Fisciano, Italy*
[11]*Istituto Nazionale di Fisica Nucleare, Sezione di Napoli, 80126 Napoli, Italy*
[12]*Faculty of Mathematics, Informatics and Natural Sciences, Department of Earth Sciences, Meteorological Institute, Universität Hamburg, Bundesstraße 55, D-20146 Hamburg, Germany*
[13]*SUPA, School of Science and Engineering, University of Dundee, Nethergate, Dundee DD1 4HN, UK*
[14]*Facultad de Ingeniería y Tecnología, Universidad San Sebastian, General Lagos 1163, Valdivia 5110693, Chile*
[15]*Facultad de Economía y Negocios, Universidad San Sebastian, General Lagos 1163, Valdivia 5110693, Chile*
[16]*Institute for Advanced Research, Nagoya University, Furo-cho, Chikusa-ku, Nagoya 464-8601, Japan*
[17]*Department of Physics, Nagoya University, Furo-cho, Chikusa-ku, Nagoya 464-8602, Japan*
[18]*Niels Bohr International Academy, The Niels Bohr Institute, Blegdamsvej 17, DK-2100 Copenhagen, Denmark*
[19]*Instituto de Astronomia y Ciencias Planetarias de Atacama, Universidad de Atacama, Copayapu 485, Copiapo, Chile*
[20]*Max Planck Institute for Astronomy, Königstuhl 17, D-69117 Heidelberg, Germany*

Downloaded from https://academic.oup.com/mnras/article-abstract/495/4/3881/5838753 by The Open University user on 22 June 2020

[21]*Department of Astronomy and Space Science, Chungnam National University, 34134 Daejeon, Republic of Korea*
[22]*Centre for Astrophysics and Planetary Science, The University of Kent, Canterbury CT2 7NH, UK*
[23]*Department of Physics, University of Rome 'Tor Vergata', Via della Ricerca Scientifica 1, I-00133 Rome, Italy*
[24]*INAF – Osservatorio Astrofisico di Torino, via Osservatorio 20, I-10025 Pino Torinese, Italy*
[25]*International Institute for Advanced Scientific Studies (IIASS), Via G. Pellegrino 19, I-84019 Vietri sul Mare (SA), Italy*
[26]*Department of Physics, Sharif University of Technology, Azadi Ave, 11155-9161 Tehran, Iran*
[27]*Las Cumbres Observatory Global Telescope, 6740 Cortona Dr., Suite 102, Goleta, CA 93111, USA*
[28]*Department of Physics, University of California, Santa Barbara, CA 93106-9530, USA*
[29]*Astrophysics Group, Keele University, Staffordshire ST5 5BG, UK*
[30]*Stellar Astrophysics Centre, Department of Physics and Astronomy, Aarhus University, Ny Munkegade 120, DK-8000 Aarhus C, Denmark*

This paper has been typeset from a TEX/LATEX file prepared by the author.

Downloaded from https://academic.oup.com/mnras/article-abstract/495/4/3881/5838753 by The Open University user on 22 June 2020